



CO₂-induced heat source changes over the Tibetan Plateau in boreal summer-Part I: the total effects of increased CO₂

Xia Qu^{1,2} · Gang Huang^{2,4,5} · Lihua Zhu³

Received: 16 February 2020 / Accepted: 23 June 2020
© Springer-Verlag GmbH Germany, part of Springer Nature 2020

Abstract

The concentration of CO₂ in the atmosphere has been increasing, but its effects on the heat source (HS) over the Tibetan Plateau (TP) are unclear. Aimed at understanding these effects, at first, present study evaluated the CMIP5 (phase 5 of the Coupled Model Intercomparison Project) models and found that their multi-model ensemble (MME) reproduces the spatial pattern of the HS over the TP during June–September (hereafter JJAS) in observation reasonably well. Then, we used the MME to investigate the response of the JJAS HS over the TP to increased CO₂. In response to increased CO₂, the JJAS HS increases significantly. In terms of the response pattern and TP-averaged results, the increase in HS is mainly contributed by the latent heating (LH), which is due to moisture increases (with the lower level stronger than the upper level) and evaporation intensification led by CO₂ change. The leading two intermodel spreads feature a nearly uniform structure and a central-southeastern TP dipole structure, respectively, and account for half of the total intermodel variance. The latent heating is mainly responsible for the spreads. The intensified radiative cooling of the atmosphere slightly dampen the TP-averaged HS increases. Over the TP, when CO₂ increases, the atmospheric column above warms. Accordingly, the net longwave radiation flux out of the atmosphere column enhances, resulting in the intensified radiative cooling over the TP.

Keywords The Tibetan Plateau · Heat source · CO₂ increase

Electronic supplementary material The online version of this article (<https://doi.org/10.1007/s00382-020-05353-9>) contains supplementary material, which is available to authorized users.

✉ Xia Qu
quxia@mail.iap.ac.cn

- ¹ Center for Monsoon System Research, Institute of Atmospheric Physics, Chinese Academy of Sciences, P. O. Box 9804, Beijing 100029, China
- ² State Key Laboratory of Numerical Modeling for Atmospheric Sciences and Geophysical Fluid Dynamics, Institute of Atmospheric Physics, Chinese Academy of Sciences, Beijing 100029, China
- ³ School of Atmospheric Sciences/Plateau Atmosphere and Environment Key Laboratory of Sichuan Province/Joint Laboratory of Climate and Environment Change, Chengdu University of Information Technology, Chengdu 610225, China
- ⁴ Laboratory for Regional Oceanography and Numerical Modeling, Qingdao National Laboratory for Marine Science and Technology, Qingdao 266237, China
- ⁵ University of Chinese Academy of Sciences, Beijing 100049, China

1 Introduction

Over the Eurasian continent, there is a huge plateau, the Tibetan Plateau (TP). Over TP, the air is cold and dry, and the solar radiation is strong. The surface air temperatures are around 0 °C, with values of 0.19 and – 0.08 °C over eastern and western parts of the TP during summer. The annual rainfall is low, ranging from 100 to 300 mm, and mainly occurs as hail. The high elevation of the TP makes it, and the atmospheric column above, a heat source (HS), especially in boreal summer, and leads to the unique climate over Asia (Li and Yanai 1996). In boreal summer, as a result of the TP heating and its insulating effect, monsoon rainfall forms over the South Asia region (Boos and Kuang 2010; Wu et al. 2012; Song et al. 2010; He et al. 2019a). The rainfall-associated latent heating (LH), along with the TP heating, firstly enhances the East Asia low-level southwesterly, reinforcing the local water vapor transport and making the northern edge of East Asia monsoon domain the most poleward (Liu et al. 2007; Lee et al. 2015; Wang and Ding 2008; He et al. 2019a); and secondly, the heating gives rise to southwesterly flow over the Arabian Sea and

Indian Peninsula, which provides moisture for South Asian monsoon rainfall and reduces the climatological temperature in the Arabian Sea region (Kitoh 2004). The combined effects of the warm atmosphere surrounding the TP and the mid-troposphere westerlies generate warm horizontal temperature advection that penetrates into the northern Pacific region. This advection plays an important role in forcing the mei-yu/baiu rain (Sampe and Xie 2010). In addition, the TP HS affects the seasonal evolution of the Asian monsoon in climatology (Ye and Wu 1998). For instance, in May, the lower sea surface temperature in the Arabian Sea induced by the TP HS stabilizes the atmosphere above and leads to a delayed onset of the monsoon in the Arabian Sea and Indian region (Abe et al. 2013; Zhao et al. 2019).

Since the Industrial Revolution, the CO₂ concentration in the atmosphere has been increasing. This has led to a rise in the surface temperature of Earth and exerted a far-reaching impact on the climate (Stocker et al. 2013). During the early-1980s to the 2000s, the HS over the TP undergoes significant weakening in all seasons in observational data (Duan and Wu 2008). The sensible heating at the surface and the net radiation flux into the TP atmospheric column mainly account for this decline. The sensible heating and net radiation flux are further led by the deceleration of the local surface wind and partly by the narrowing of the surface–air temperature difference (Duan and Wu 2008, 2009). Given the interference of aerosol, natural forcing and internal climate variability, the individual contribution of CO₂ is difficult to separate in observational data. Thus, simulation is a reasonable tool for studying the contribution.

The previous outputs of the CMIP5 (phase 5 of the Coupled Model Intercomparison Project) models have revealed that, in a warmer climate, it is evident that the components of the HS, such as the LH of the atmospheric column, the energy fluxes at the surface and top of the atmosphere (see Sect. 2.3 for detailed information), may change. Under representative concentration pathway scenarios in which the anthropogenic forcing is stronger than that in present-day climate (Riahi et al. 2011; Thomson et al. 2011), the surface over the TP is warmer (Su et al. 2013; Hu et al. 2015), implying an intensification of the surface upwelling longwave radiation, the surface sensible heating and surface LH. Accordingly, the atmospheric column over the TP would become warmer, indicating a rise in the downwelling longwave radiation at surface and the upwelling longwave radiation at top of atmosphere. In relation to this, the rainfall, as well as the LH, over the TP has been projected to be enhanced (Su et al. 2013; Hu et al. 2015), which may strengthen the East Asian monsoon southwesterly (He et al. 2019b). Furthermore, in response to increased CO₂, the snow cover over the TP declines and the glaciers retreat, leading to a reduction in surface albedo (Qu et al. 2019; Yao et al. 2012). Consequently, the upwelling shortwave

radiation at the surface tend to become weakened. However, the results of many of these studies have been based on the Representative Concentration Pathway scenarios. Although CO₂ increase is the main external forcing in these scenarios, concurrently, the aerosols are largely reduced (Riahi et al. 2011; Thomson et al. 2011). Evidences show that the change in aerosol forcing has profound influences on South Asian monsoon precipitation, climate in East Asian arid and semiarid regions and the TP, and that its effect is non-negligible (Huang et al. 2014, 2019; Kang et al. 2016; Li et al. 2015; Wang et al. 2019). Thus, to clearly understand the HS response to global warming, the first step is to determine how the HS responds to increased CO₂ over the TP and which components are dominant.

The remainder of the paper is organized as follows: Sect. 2, the data and methods are introduced. Section 3 presents the results regarding the HS response to increased CO₂ over the TP. Section 4 investigates the responses of the HS components to increased CO₂ over the TP and the associated causes. In Sects. 5 and 6 examine the contributions of the components to the spatial pattern and intermodel spread of the HS response, respectively. Finally, a summary and discussion are provided in section.

2 Data and methods

2.1 Data

The key aspects of present study are calculation of HS, model evaluation and moisture budget. So far, the number of Coupled Model Intercomparison Project phase 6 (CMIP6) models which contain available data associated with those key aspects is 17. The corresponding number is 30 for CMIP5 dataset. So, the present study uses CMIP5 monthly outputs (Taylor et al. 2012), the details of which are provided in Table 1. The experiments used were: (1) 1%CO₂ experiment (the CO₂ concentration in the models increases 1% per year until the concentration had quadrupled) and (2) historical experiment (observed forcings, such as anthropogenic and natural forcings, from the mid-19th century to 2005 are used to force the models). The present study only uses the first run in each model (termed r1i1p1). We choose 1%CO₂ rather than abrupt 4xCO₂ experiment for: (1) the gradual increase of CO₂ concentration in 1%CO₂ experiment is similar to the situation in present climate. (2) in abrupt 4xCO₂ experiment (the CO₂ concentration is fixed except the first several years), some climate processes, such as extratropical sensible heat transport, are different to those in 1%CO₂ experiment (Held and Soden 2006).

To evaluate the model performance, the following observational and reanalysis data were used: (1) the Global Precipitation Climatology Centre (GPCC) dataset (Becker et al.

Table 1 Information on the climate models used in this study Source: http://cmip-pcmdi.llnl.gov/cmip5/docs/CMIP5_modeling_groups.pdf

No.	Model ID (no.)	Modeling center (or group)
1	ACCESS1.0	Commonwealth Scientific and Industrial Research Organization and Bureau of Meteorology, Australia
2	ACCESS1.3	
3	BCC-CSM1.1	Beijing Climate Center, China Meteorological Administration
4	BCC-CSM1.1 m	
5	BNU-ESM	College of Global Change and Earth System Science, Beijing Normal University
6	CanESM2	Canadian Centre for Climate Modelling and Analysis, Canada
7	CCSM4	National Center for Atmospheric Research, USA
8	CESM1-BGC	
9	CNRM-CM5	Centre National de Recherches Météorologiques, Centre Européen de Recherche et de Formation Avancée en Calcul Scientifique, France
10	CNRM-CM5-2	
11	CSIRO-Mk3.6.0	Commonwealth Scientific and Industrial Research Organization in collaboration with Queensland CSIRO-QCCCE CSIRO-Mk3.6.0 Climate Change Centre of Excellence, Australia
12	FGOALS-s2	LASG, Institute of Atmospheric Physics, Chinese Academy of Sciences and CESS, Tsinghua LASG-CESS FGOALS-g2 University, China
13	GFDL-CM3	NOAA Geophysical Fluid Dynamics Laboratory, USA
14	GFDL-ESM2G	
15	GFDL-ESM2M	
16	GISS-E2-H	NASA/GISS (Goddard Institute for Space Studies), USA
17	GISS-E2-R	
18	HadGEM2-ES	Met Office Hadley Centre, UK
19	INM-CM4	Institute for Numerical Mathematics, Russia
20	IPSL-CM5A-LR	Institut Pierre Simon Laplace, France
21	IPSL-CM5A-MR	
22	IPSL-CM5B-LR	
23	MIROC-ESM	Atmosphere and Ocean Research Institute (The University of Tokyo), National Institute for Environmental Studies, and Japan Agency for MIROC5 Marine-Earth Science and Technology, Japan
24	MIROC5	
25	MPI-ESM-LR	Max Planck Institute for Meteorology
26	MPI-ESM-MR	
27	MPI-ESM-P	
28	MRI-CGCM3	Meteorological Research Institute
29	NorESM1-M	Norwegian Climate Centre
30	NorESM1-ME	

2013); (2) the Global Precipitation Climatology Project (GPCP) monthly precipitation analysis (Adler et al. 2003); (3) the NCEP–DOE AMIP-II reanalysis (hereafter NCEP2; Kanamitsu et al. 2002); and (4) the JRA-55 reanalysis (Kobayashi et al. 2015); (5) Northern Hemisphere EASE-Grid Weekly Snow Cover and Sea Ice Extent (Robinson et al. 1993).

2.2 Methods

When investigating the responses, we used 1%CO₂ experiment, the length of which is 140 years. The response to increased CO₂ is defined as the climatology during years 1–20 subtracted from that during years 121–140. For short, we named the response as “1%CO₂” (Note it is different to the experiment name “1%CO₂” in Sect. 2.1). When

evaluating the model performance, unless stated, we focused on the period of 1980–2005 in the historical simulations, observational data and reanalysis data.

The multi-model ensemble (MME) method was used to reveal the overall performance and response of the models. The 95% confidence intervals (CIs) among the models were used to identify the significance of the signal. To facilitate the analysis of the MME and CIs, we interpolated the data onto a 1.0° × 1.0° grid by using bilinear interpolation. In the area average, the interpolation was not used.

An intermodel empirical orthogonal function (EOF) method was employed to study the intermodel spread. Traditionally, the EOF analysis is performed on a variable of 3-dimension (one dimension is time; Du et al. 2009; Wang and Ding 2008; Wang et al. 2001). In intermodel EOF analysis, we regard the spatial pattern of the 1st model as the

result of “time step 1”; the spatial pattern of 2nd model as “time step 2”, and so on. The EOF results of this 3-dimension variable are the spatial patterns of the intermodel diversity around the MME mean result. For a given model, the corresponding principle component is the magnitude of the feature departed from the MME mean.

2.3 Calculation of the HS

The calculation of the HS was based on precipitation and energy fluxes (Duan and Wu 2008; Li and Yanai 1996). The HS of the column was

$$HS = LP + SH + R_{\text{net}},$$

where $L = 2,500,632 \text{ J kg}^{-1}$, P , SH , R_{net} are is the precipitation, the surface sensible heating and the net radiation flux into the atmospheric column, respectively.

The net radiation flux into the atmospheric column was

$$R_{\text{net}} = L_s \uparrow - L_s \downarrow + S_s \uparrow - S_s \downarrow + S_t \downarrow - L_t \uparrow - S_t \uparrow,$$

where L and S represent the longwave and shortwave radiation, respectively; the symbols \uparrow and \downarrow mean upwelling and downwelling radiation, respectively; and the subscript “s” and “t” mean radiation flux at the surface and the top of the atmosphere.

2.4 Performance of the CMIP5 MME and target months

Before investigating the response of the HS, the overall performance of the CMIP5 models are evaluated. The

calculation of the HS was based on the precipitation and energy flux. The precipitation datasets used were GPCC and GPCP, while the reanalysis datasets employed were JRA-55 and NCEP2. There were four combinations of observations, and the similarities between the CMIP5 MME and the HS based on the four combinations of observations are demonstrated by Taylor diagrams (Taylor 2001) in Fig. 1. Note that, as the present study focused on the response of the CMIP5 MME to increased CO_2 , in this paper we demonstrate the similarity between the MME and the observation/reanalysis data. Regardless of the observational HS is calculated based on GPCC or GPCP, the HS similarities of the CMIP5 MME to the observation/reanalysis data are almost the same. Meanwhile, if the observational HS is calculated based on different reanalysis, the similarities of the CMIP5 MME to the observation/reanalysis data show large differences, with the CMIP5 MME results being closer to those of JRA-55. In all kinds of data combination, the results for June to September were closest to the CMIP5 MME among all the months. For JRA-55 and the precipitation dataset, the pattern correlation coefficients from June to September were greater than 0.9, while for NCEP2 and the precipitation dataset they were no less than 0.7. Besides, in these months, the standard deviations were found to be reasonable. Thus, in the following analysis, we only focus on the HS change from June to September (hereafter JJAS).

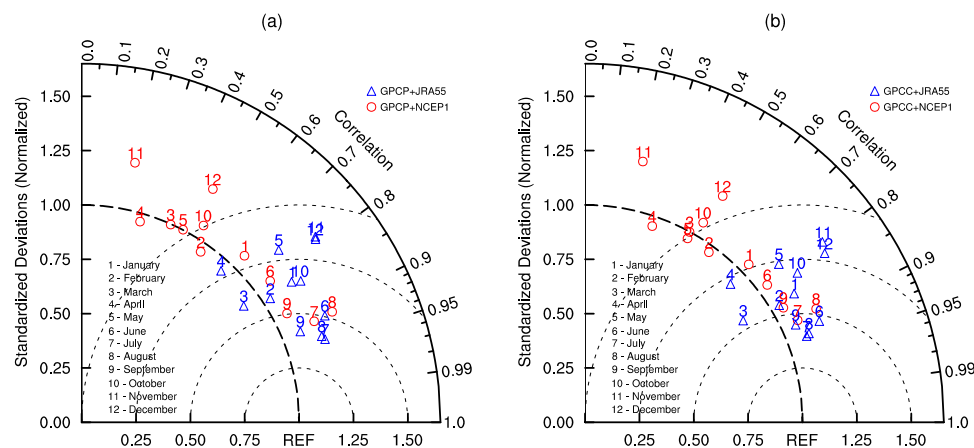


Fig. 1 Taylor diagrams displaying the reproducibility of the HS pattern by the CMIP5 MME over the TP during 1980–2005. In **a**, red circles (blue triangles) are the results of the CMIP5 MME against the HS computed by using GPCP and NCEP2 (JRA-55) reanalysis data; in **b**, red circles (blue triangles) are the results of the CMIP5 MME against the HS computed by using GPCC and NCEP2 (JRA-

55) reanalysis data. The numbers 1–12 denote January to December, respectively. The ratio of the standardized deviation and the spatial correlations are indicated by the radial distance and radial angle, respectively. The distance to “REF” is the center root-mean-square error

3 HS response to increased CO₂

The JJAS HS is enhanced in response to increased CO₂. Figure 2 displays the response of the HS over the TP in June, July, August and September, and the JJAS mean results. In these 4 months, the TP is dominated by a significantly increased HS. In general, large increase mainly resides in the southern TP and the increased HS gradually weakens from south to north. The largest increase ($\sim 124 \text{ W m}^{-2}$) occurs over the southern TP near 90°E in July (Fig. 2b). In September, the area with slightly decreased HS west/northwest of the TP is the largest among the 4 months (Fig. 2d). This may due to the reduction of response magnitudes of the LH and sensible heating from July to September. The JJAS-mean response of the HS is similar to that in July, but the amplitude is slightly weaker in general. Besides, the TP-averaged HS change is demonstrated (noting that this area average only considers those grid boxes with altitude at or above 3000 m over the TP). The averaged HS displays the largest enhancement in July and the lowest in September (20 and 11 W m^{-2} , respectively; Fig. 2f). The enhancements of the 4 months all reach the 95% significance level.

The pattern of the climatological HS (JJAS-mean HS in historical simulation during the period of 1980–2005) does not determine the pattern of this HS response over the TP. For individual models, the spatial correlation coefficients of the HS response with the climatological of the HS span from -0.65 to 0.85 (95% CI 0.28–0.56).

The topography of the TP is complex, which raises the question: does the representation of the topography in

the models affect the HS response? Our results suggest it does not. In this respect, we investigated the relationship between the model resolution and the JJAS HS response to increased CO₂, and no direct connection was found between them, either in magnitude or pattern (Fig. s1 and s2 in supplemental material).

4 TP-averaged response

As the HS is the net effect of the latent heating, sensible heating at surface and net radiation fluxes of the atmosphere, we next investigate these components, one by one, beginning with the TP-averaged results. Figure 3 demonstrates the area average of JJAS-mean response of the HS and associated components in 1%CO₂ results over the TP. The average only used grid boxes whose altitudes are at or above 3000 m. The downwelling longwave and shortwave radiations as well as the upwelling longwave and shortwave radiations contribute to heat loss of the atmosphere column. To facilitate the understanding of the budget of the HS, these radiation values are multiplied by -1 in Fig. 3. So positive (negative) values mean heat gain (loss) of the atmospheric column.) In response to increased CO₂, the atmosphere over the TP warms. Due to the limited supply of moisture, the relative humidity is likely to reduce (Byrne and O’Gorman 2016; O’Gorman and Muller 2010); along with the slightly weakened ascendance led by muted hydrological cycle to global warming (Endo and Kitoh 2014; Held and Soden 2006), total cloud amount overall decreases over the TP and the cloud–radiation feedback changes (Kamae et al. 2016), which may in turn affect the local HS. To determine the

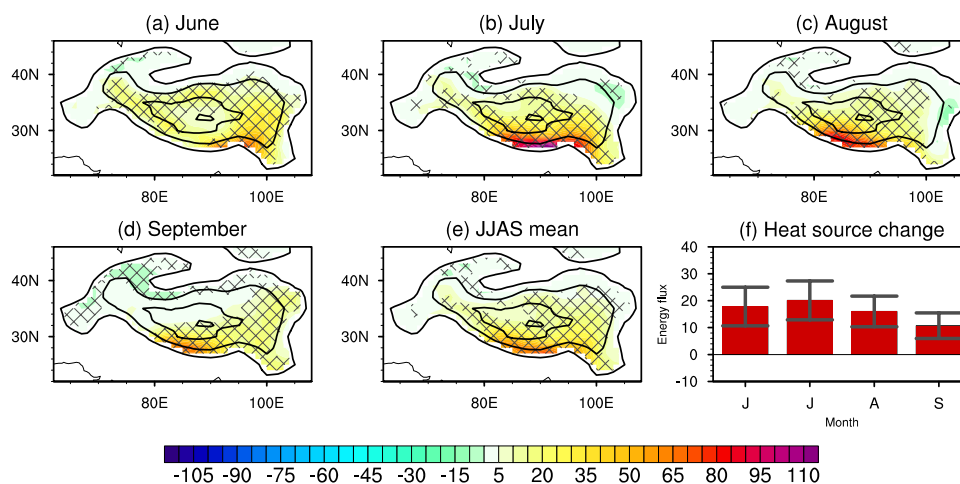


Fig. 2 The responses of June, July, August, September and June–September mean HS (color shading, a–e) and the TP-averaged HS response (f) from June to September for the 1%CO₂ results. Only those grid boxes with elevations at or above 3000 m were used to calculate the TP average. Units: W m^{-2} . The responses are the MME

results. In a–e, the contours represent the elevations of 1500, 3000, 5000 and 6000 m; the lattices indicate the response reaching the 95% significance level. In f, the error bars denote the 95% CIs of the changes based on intermodel spread

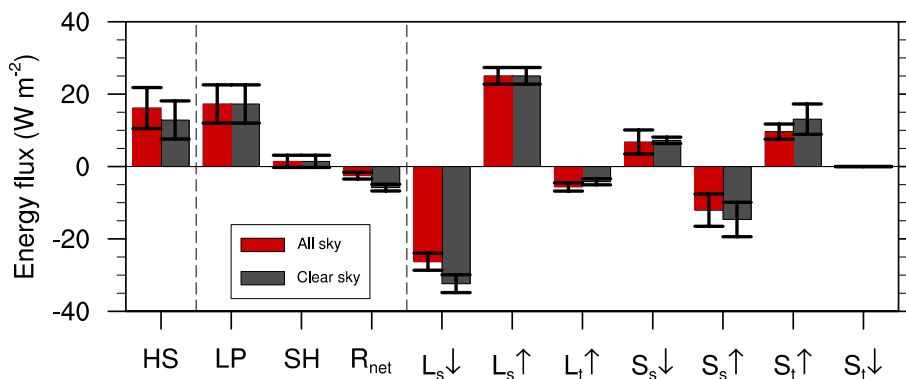


Fig. 3 The JJAS-averaged response in each term of the HS, as well as the radiation fluxes, in the 1%CO₂ experiment over the TP. Only those grid boxes with elevations at or above 3000 m over the TP were used to compute the average. The downwelling longwave and shortwave radiations and the upwelling longwave and shortwave radiations

are multiplied by -1. So positive and negative values indicate heat gain and loss of the atmospheric column, respectively. Units: W m⁻². The red and gray bars denote the all-sky and clear-sky results, respectively. The error bars represent the 95% CIs of the changes

potential influence of cloud–radiation feedback on the HS, clear-sky radiation is used (displayed as gray bars). The following clear-sky variables were available: downwelling longwave radiation, downwelling shortwave radiation and upwelling shortwave radiation at the surface, and upwelling shortwave and longwave radiation at the top of the atmosphere. The other energy fluxes are the same as those in the all-sky results when we computed the clear-sky HS.

During JJAS, the TP HS of the CMIP5 MME increases by 16.2 W m⁻² in the 1%CO₂ result, and then it drops to 12.9 W m⁻² when the cloud–radiation feedback is absent. This drop, however, is statistically insignificant if the intermodel spread is taken into consideration (Fig. 3). Among the components contributing to the HS change, the role of LH and net radiation are significant. In the following subsections, we investigate the contributions of the two. The sensible heating at the surface are not analyzed because its response was statistically insignificant.

4.1 LH

The LH in the atmospheric column is the most important component to the HS change. The TP-averaged LH of the CMIP5 MME increases by 17.3 W m⁻² in the 1%CO₂ results. To further study the effect of increased CO₂ on the LH change, the moisture budget was employed. Based on Luo and Yanai (1984) and Chou et al. (2009), the LH (which equals to LP) change can be written as

$$LP' \approx \langle -L\bar{\mathbf{V}} \cdot \nabla q' \rangle + \langle -L\mathbf{V}' \cdot \nabla \bar{q} \rangle + \langle -L\bar{\omega} \partial_p q' \rangle + \langle -L\omega' \partial_p \bar{q} \rangle + LE,$$

where $L = 2,500,632 \text{ J kg}^{-1}$; \mathbf{V} , ω , q and E are the horizontal wind, pressure velocity, specific humidity and evaporation, respectively; an overbar and prime indicate the climatology

and change, respectively; and angle brackets, $\langle \rangle$, represent mass integration from the surface to 100 hPa.

The results of moisture budget (Fig. 4) show that the LH increase is mainly contributed by the increased vertical gradient of humidity. It can trace back to CO₂ increasing. The increasing induces a warmer in global atmosphere, including that above the TP. According to the Clausius–Clapeyron equation, the saturated water vapor pressure increases. Accompanied by the enhanced evaporation which supplies the moisture, the atmosphere becomes wetter. The humidity increases are larger at lower than upper levels in the troposphere, yielding the enhanced vertical gradient of humidity. The climatological ascendance over the TP transports more moisture upwards and results in intensification of condensational heating.

The change in surface LH released to atmosphere also favors the LH increase in atmosphere. The MME LH at the surface released to the atmosphere increases significantly by 8.5 W m⁻² during JJAS in the 1%CO₂ results (Fig. 4h). The surface LH exchange is linked to surface evaporation. Based on the formula for the LH over a surface (Du et al. 2009), the anomaly of potential evaporation over land is written as

$$E' = E_1 + E_2 + E_3 + E_4 + E_5,$$

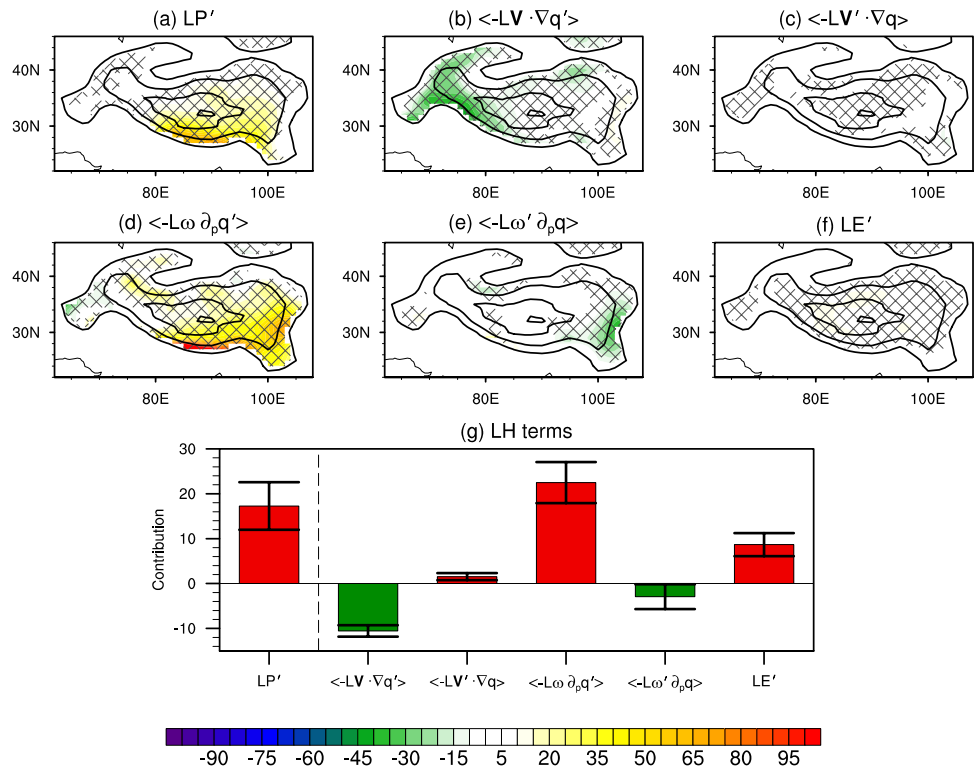
where

$$E_1 = \bar{\rho}_a C_E \bar{W} \left[q_s(\bar{T} + T') - q_s(\bar{T}) \right],$$

$$E_2 = \bar{\rho}_a C_E \bar{W} \left[-\overline{RH} q_s(\bar{T}_a + T'_a) + \overline{RH} q_s(\bar{T}_a) \right],$$

$$E_3 = \bar{\rho}_a C_E \bar{W} \left[-RH' q_s(\bar{T}_a) \right],$$

Fig. 4 The JJAS-average of the moisture budget terms over the TP (color shading, **a–f**) and the area average of the terms (**g**) for the 1%CO₂ results. The results are the mass integration from the surface to 100 hPa. Only those grid boxes with elevation at or above 3000 m were used to calculate the average. Units: W m⁻². The responses are the MME results. In **a–e**, the contours represent elevations of 1500, 3000, 5000 and 6000 m; the lattices indicate the response reaching 95% significance level. In **g**, the error bars denote the 95% CIs of the changes based on intermodel spread



$$E_4 = \rho'_a C_E \bar{W} \left[q_s(\bar{T}) - \overline{\text{RH}} q_s(\bar{T}_a) \right], \text{ and}$$

$$E_5 = \bar{\rho}_a C_E \bar{W}' \left[q_s(\bar{T}) - \overline{\text{RH}} q_s(\bar{T}_a) \right],$$

in which ρ_a is the surface air density, C_E is the transfer coefficient, W is the 10-m wind speed, q_s is the saturated specific humidity, T is the surface temperature, T_a is the air temperature at the surface, and RH is the relative humidity.

The terms E_1, E_2, E_3, E_4 and E_5 are respectively the contributions of change in surface temperature, surface air temperature, relative humidity, air density and surface wind speed to the changes in potential evaporation. Figure 5 displays the contributions of the terms to changes in JJAS potential evaporation. The changes in potential evaporation over the TP are mainly led by CO₂-induced surface warming, while the surface air warming acts to partly offset the increases in potential evaporation. The contribution of the other terms is negligible. The net effect of the terms is towards the increase

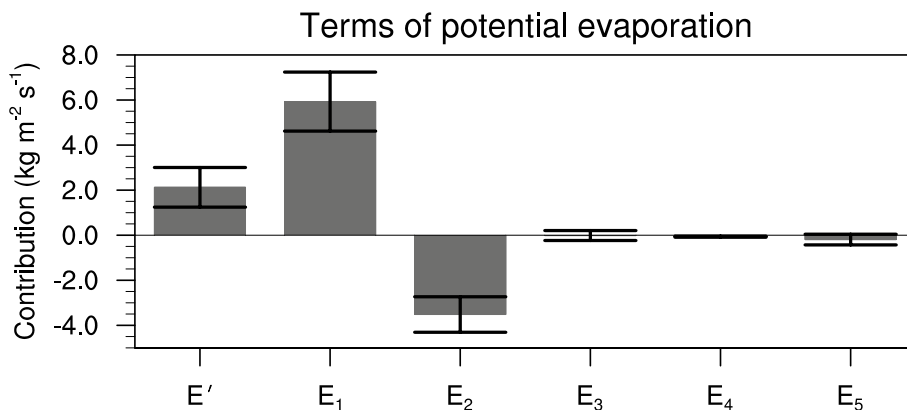


Fig. 5 The TP-averaged terms of JJAS potential evaporation for the 1%CO₂ results. Only those grid boxes with elevations at or above 3000 m over the TP were used to calculate the area average. The results have been divided by the transfer coefficient C_E . Units: kg m⁻²

s⁻¹. The error bars represent the 95% CIs of the changes. The following models were not used in the calculation because of their lack of surface relative humidity data: bcc-csm1-1, CCSM, CESM1-BGC, CSIRO-Mk3-6-0, MPI-ESM-LR, MPI-ESM-MR, MPI-ESM-P

in potential evaporation, which favors the enhancement of the actual evaporation and finally the surface LH flux to the atmosphere. The finding that the CO₂-induced surface warming mainly contributes to the potential evaporation over the TP is confirmed by the results in Laine et al. (2014), which focus on global warming-induced evaporation change on global scale.

4.2 Radiation fluxes

Concurrently, the net radiation flux (defined in Sect. 2.3) acts to dampen the HS increase at the TP surface. The climatological JJAS net radiation flux cools the atmosphere (usually named as radiative cooling). The net radiation flux out of the atmosphere column during year 1–20 in the MME of 1%CO₂ experiment is 73.5 W m⁻². It increases by 2.5 W m⁻² in response to increased CO₂ in the 1%CO₂ results (Fig. 3), corresponding slightly intensification of the cooling effect. The clear-sky net radiation flux increases by 5.8 W m⁻², indicating that the participation of cloud-radiation feedback contributes to an increase in the HS (heating enhancement) over the TP.

The radiative cooling mainly relies on longwave radiation fluxes. The net longwave radiation flux into the atmosphere column above the TP decreases by 6.9 W m⁻². In the following, the longwave radiation fluxes are investigated one by one:

The surface downwelling longwave radiation flux The radiation flux at the TP surface increases significantly. It contributes to the intensification of radiative cooling but the weakening of the HS over the TP. In the 1%CO₂ results, the area average of the radiation over the TP increases by 26.3 W m⁻² in MME results (Fig. 3). The longwave radiation displays a uniform increase over the TP (Fig. 6a). Excluding the cloud-radiation feedback, the increase is higher (32.4 W m⁻²; Fig. 3), indicating that the atmospheric warming, which is a result of increased CO₂, mainly accounts for the enhancement of the downwelling longwave radiation at the TP surface and that the cloud-radiation feedback slightly weakens the enhancement (Figs. 3, 6b, c). In response to increased CO₂, due to the decline in relative humidity in the atmosphere, the total cloud amount reduces 2.5–3.3% (95% CI) in the 1%CO₂ results. The reduction leads to the decrease in downwelling longwave radiation at the TP surface and slightly hampers the increase in the downwelling longwave radiation caused by atmospheric warming.

The surface upwelling longwave radiation flux The radiation flux at the TP surface increases significantly. It partly counteracts the increase in radiative cooling and favors the enhancement of TP HS. In the MME of the 1%CO₂ results, the TP-averaged radiation increases by 25.0 W m⁻² (Fig. 3). Following Stefan–Boltzmann's law, the radiation flux of an idealized black body is

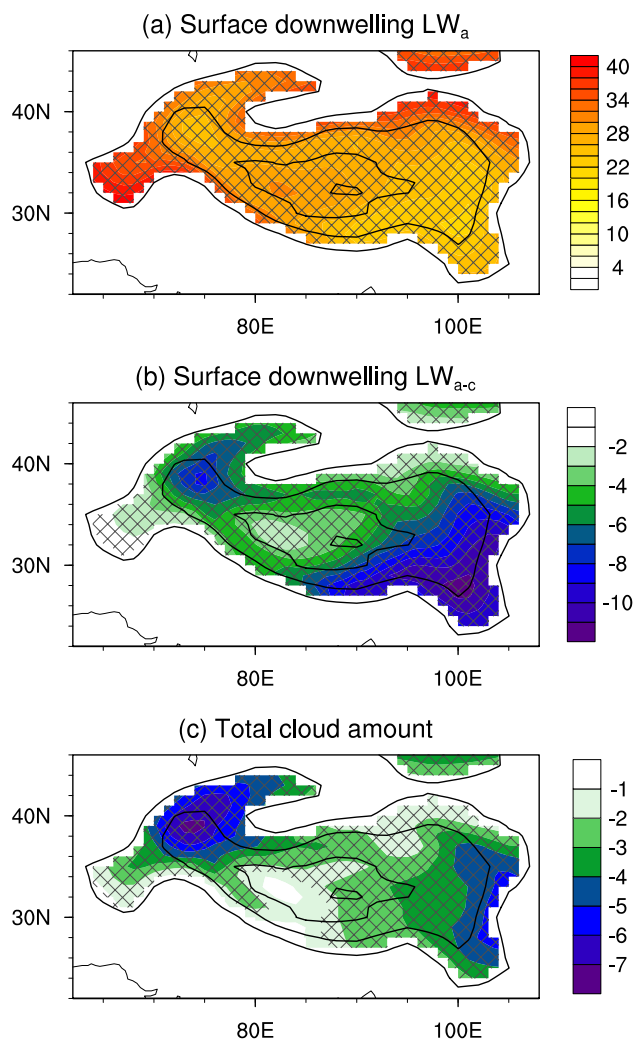


Fig. 6 The MME response (color shading) of the downwelling longwave radiation at the surface (**a**, **b** units: W m⁻²) and total cloud amount (**c** units: %) during JJAS for the 1%CO₂ results. Panel **a** is the all-sky results; **b** is the results of all-sky minus clear-sky. The contours represent elevations of 1500, 3000, 5000 and 6000 m; the latitudes indicate the response reaching the 95% significance level

$$B(T) = \delta T^4,$$

where $\delta = 5.67 \times 10^{-8} \text{ W m}^{-2} \text{ K}^{-4}$. For the TP surface, δ may not be equal to this value. Providing the change in surface upwelling longwave radiation is solely contributed by temperature, then δ does not change, and the relative changes of upwelling longwave radiation flux at the surface may equal those of T^4 . The relative change of the downwelling longwave radiation at the surface and the biquadratic surface temperature for the 1%CO₂ results are displayed in Fig. 7. The relative change of the downwelling longwave radiation at the surface generally displays an east–west gradient. The largest (lowest) increase resides over the western (southeastern) TP. The relative change of T^4 shows nearly the same

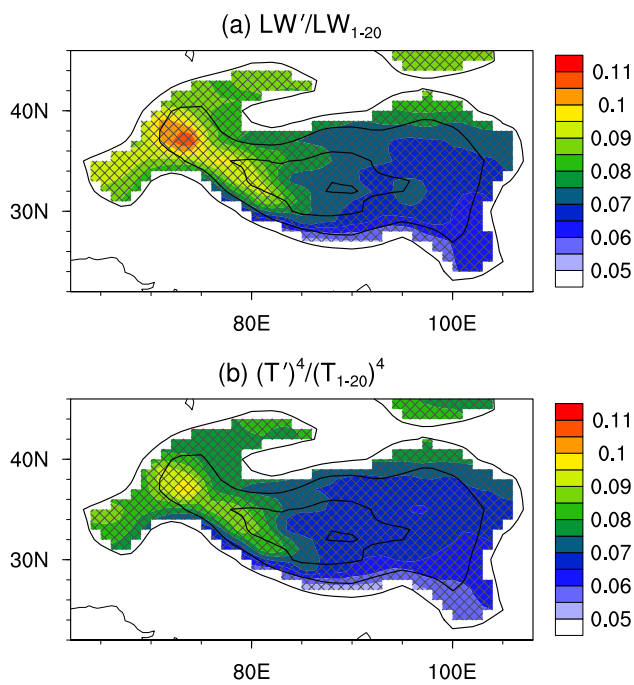


Fig. 7 The MME relative change (color shading) of the downwelling longwave radiation at the surface (a) and the biquadratic surface temperature (b) during JJAS for the 1%CO₂ results. The contours represent elevations of 1500 m, 3000 m, 5000 m and 6000 m; the lattices indicate the response reaching the 95% significance level

pattern as that of the downwelling longwave radiation at the surface, with a spatial correlation coefficient of 0.94. The magnitudes of the relative changes are close. The area average of the relative change of the downwelling longwave radiation at the TP surface is 6.6–8.4% (95% CI), while the value is 6.5–7.7% (95% CI) for the biquadratic surface temperature. Both the results of the pattern and the magnitude indicate that surface warming leads to the change in the upwelling longwave radiation over the TP. This surface warming is a product of increased CO₂.

The outgoing longwave radiation flux at the top of the atmosphere In response to increased CO₂, this radiation flux strengthens significantly. Alike the downwelling longwave radiation flux, it contributes to the strengthening of radiative cooling but the weakening of the HS over the TP. In CMIP5 MME of the 1%CO₂ results, the TP-averaged radiation increases by 5.6 W m⁻² (Fig. 3). The response of the longwave radiation features a uniform increase over the TP (Fig. 8), with a slightly larger increase over the western TP. The outgoing longwave radiation at the top of the atmosphere is hard to evaluate, mainly stemming from the difficulty in the evaluation of the longwave radiation emitted from the atmospheric column above the TP. Besides, the atmospheric column may slightly absorb the longwave radiation emitted from the TP surface. In our case, the CO₂-induced warming at the TP surface and the atmospheric

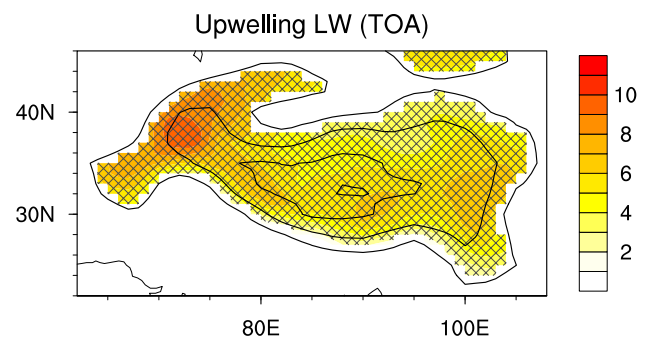


Fig. 8 The MME response (color shading) of JJAS upwelling longwave radiation (units: W m⁻²) at the top of the atmosphere for the 1%CO₂ results. The contours represent elevations of 1500, 3000, 5000 and 6000 m; the lattices indicate the response reaching the 95% significance level

column above both favor the increase in outgoing longwave radiation at the top of the atmosphere. Meanwhile, the inclusion of cloud–radiation feedback exerts little influence on the response of the outgoing longwave radiation (Fig. 3).

Unlike the net longwave radiation flux, the net shortwave radiation flux into the atmosphere column above the TP increases by 4.5 W m⁻², partly offsetting the intensification of radiative cooling. The detailed responses of the shortwave radiation fluxes are demonstrated in Sect. 8.

To summarize, over the TP, when CO₂ increases, the enhanced LH of the atmosphere, led by the moisture increases (with lower levels stronger than upper levels) and intensified evaporation, is the main cause of the TP-averaged HS increase. The contribution of the sensible heating is insignificant. The radiative cooling of the atmosphere slightly enhances and partly cancels out the TP-averaged HS increase. This enhancement of radiative cooling is mainly led by atmospheric warming over the TP.

5 Contribution to the spatial pattern

Having investigated the HS components, we now have an impression of which terms are important in their contribution to the TP-averaged response of the HS to increased CO₂. However, the contributions of the terms to the spatial pattern are not yet clear. To investigate this, two aspects need to be considered: the spatial pattern correlation and the spatial standardized deviation. Coincidentally, it is possible to display these two aspects in a Taylor diagram: the ratio of the standardized deviation and the spatial pattern correlations are indicated by the radial distance and radial angle, respectively. Figure 9 is a Taylor diagram displaying the contribution of the components to the spatial pattern of the HS over the TP.

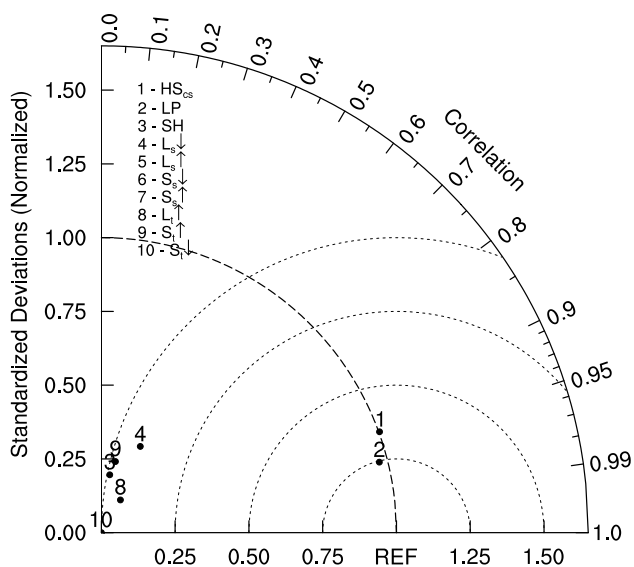


Fig. 9 Taylor diagram displaying the similarity of the heating and energy fluxes to the HS. Only MME results are shown. The numbers 1–10 denote the clear-sky HS, LH, surface sensible heating, surface downwelling longwave radiation, surface upwelling longwave radiation, surface downwelling shortwave radiation, surface upwelling shortwave radiation, upwelling longwave radiation at the top of the atmosphere, upwelling shortwave radiation at the top of the atmosphere, and the downwelling shortwave radiation at the top of the atmosphere, respectively. The ratio of the standardized deviation and the spatial correlations are indicated by the radial distance and radial angle, respectively. The distance to “REF” is the center root-mean-square error. The results of surface upwelling longwave radiation, surface downwelling shortwave radiation and surface upwelling shortwave radiation are not displayed as their spatial correlation results are negative

Among the compared variables, the one most approaching HS (REF) is HS_{cs} (clear-sky HS). For the MME results, its spatial correlation coefficient with HS is approaching 0.94 and the ratio of the standardized deviation is 1.00 (Fig. 9). The individual models display similar results: the 95% CI of the spatial correlation coefficient is (0.99, 1.00), and that of the ratio of the standardized deviation is (0.94, 0.96) (see Table 2). This means the effect of cloud–radiation feedback on the response pattern of the TP HS is negligible.

The variable which is second-closest to HS (REF) is LH. For the MME results, its spatial correlation coefficient with the HS is 0.97 and the ratio of the standardized deviation is 0.97 (Fig. 9). In individual models, the results are similar. The spatial correlation coefficients of the individual models are slightly lower (95% CI 0.92–0.95; Table 2). The ratio of the standardized deviation of the individual model results are slightly larger (95% CI 0.94–1.00; Table 2). Despite the negligible discrepancies between the MME and individual models, it does not change the fact that LH is the most important contributor to the HS response over the TP when CO₂ increases.

For the remaining variables, their contributions are weak. Their spatial correlation coefficients with the HS are less than 0.52 (Fig. 9) but, most importantly, their ratios of standardized deviation are lower than 0.42. Even for upwelling shortwave radiation at the TP surface, whose ratio of standardized deviation is 0.42, its spatial correlation coefficient with the HS is –0.02 (this result is not displayed in Fig. 9 as the negative correlation coefficient is not displayed in the Taylor diagram). For the surface downwelling shortwave radiation, whose ratio of standardized deviation is not so small (0.36), the spatial correlation coefficient is –0.06 (also not displayed in Fig. 9 since the negative correlation coefficient is not displayed in the Taylor diagram). In

Table 2 The 95% CI of the spatial correlation coefficients and the ratios of standardized deviation at the TP surface among the CMIP5 models

	Spatial correlation coefficients	Ratios of standardized deviation
HS _{cs}	(0.99, 1.00)	(0.94, 0.96)
LP	(0.92, 0.95)	(0.94, 1.00)
Surface sensible heating	(–0.03, 0.21)	(0.24, 0.32)
Surface downwelling longwave radiation	(–0.02, 0.21)	(0.24, 0.30)
Surface upwelling longwave radiation	(–0.30, –0.07)	(0.22, 0.27)
Surface downwelling shortwave radiation	(0.20, 0.43)	(0.35, 0.48)
Surface upwelling shortwave radiation	(–0.38, –0.20)	(0.30, 0.51)
Upwelling longwave radiation at top of atmosphere	(0.35, 0.53)	(0.13, 0.17)
Upwelling shortwave radiation at top of atmosphere	(–0.12, 0.14)	(0.29, 0.39)
Downwelling shortwave radiation at top of atmosphere	(0.06, 0.23)	(0.00, 0.00)

The spatial correlation coefficients were computed by using the response results between the given variable (1st column) and the HS; the ratio of standardized deviation is the spatial standardized deviation of the responses of the given variable (1st column) divided by that of the HS response. Only data in grid boxes with elevations at or above 3000 m were included in the computation

individual models, the overall ratios of standardized deviation and spatial correlation coefficient for these remaining variables are remarkably lower than those for LH (Table 2). Thus, variables other than LH make a quite limited contribution to the HS increase. In other words, for the response pattern of the HS, the LH enhancement over the TP is the dominant factor.

6 Model spread

The TP-averaged response of the HS to increased CO₂ displays intermodel spread (Fig. 3). The TP average represents the overall change over the TP. Still, it is not clear whether the most prominent spread feature among the CMIP5 models is spatially uniform. To study the spread, an intermodel EOF method was employed. First, the EOF analysis was applied to the HS response among the CMIP5 models. Several important intermodel modes, as well as their principle components, were obtained. Figure 10 displays the intermodel regression of the variables against the normalized leading principle component. The regression of the HS response reflects that the leading intermodel spread is a mode with nearly uniform deviation across the TP to the MME results (Fig. 10a). This mode accounts for 30.7%

of the total intermodel variance. Similar to the results in Sect. 5, the LH is mainly responsible for this kind of intermodel spread (Fig. 10c) and the role of cloud–radiation feedback is negligible (Fig. 10b). The surface downwelling shortwave radiation, and the upwelling shortwave radiation at the top of atmosphere promote the uniform-like spread slightly (Fig. 10e, h, k), while the surface upwelling shortwave radiation partly offset this kind of spread (Fig. 10f, i). The magnitudes, meanwhile, are small relative to that of LH.

The second mode of the intermodel EOF features a dipole structure, with the central TP and the southeastern TP in a seesaw structure (see Fig. s3 in supplemental material). This mode represents a kind of model deviation that is positive HS anomaly over the central TP and negative HS anomaly over the southeastern TP, over reversed pattern, around the MME HS response in individual models. This mode accounts for 22.9% of the total intermodel variance. Similar to the leading intermodel mode, the LH is the main contributor. The other modes are not discussed as their variances account for no more than 11.0%.

The first two modes account for 53.6% of the total variance, and the LH is the most important contributor (among the components) of both modes. Thus, the LH is the most important among the components contributing to the intermodel spread of the HS over the TP.

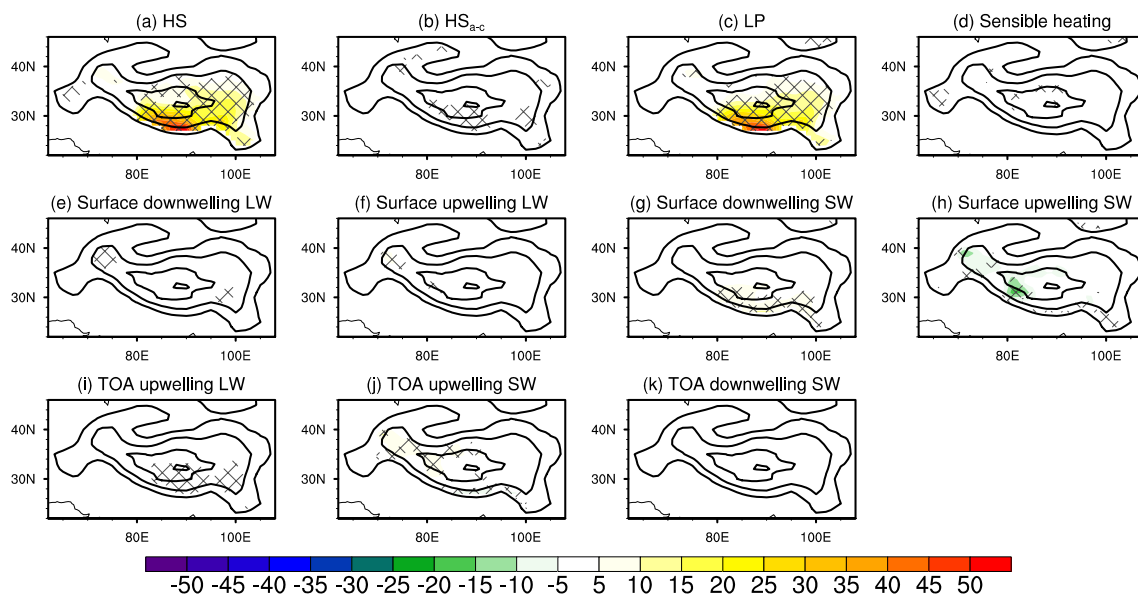


Fig. 10 The intermodel regression (color shading) onto the normalized 1st Principle Component yielded by the intermodel EOF of HS responses: **a** the HS response; **b** the response of the difference in the HS between all sky and clear sky; **c** LH; **d** sensible heating; **e** surface downwelling longwave radiation; **f** surface upwelling longwave radiation; **g** surface downwelling shortwave radiation; **h** surface upwelling

shortwave radiation; **i** upwelling longwave radiation at the top of the atmosphere; **j** upwelling shortwave radiation at the top of the atmosphere; and **k** downwelling shortwave radiation at the top of the atmosphere. Units: W m^{-2} . The contours represent elevations of 1500, 3000, 5000 and 6000 m; the lattices indicate the regression reaching the 95% significance level

7 Summary and discussion

Using the historical experiment of CMIP5, we found that the CMIP5 MME is capable of reproducing the climatological features of the HS (calculated based on GPCP, GPCC, JRA-55 and NCEP2 data) over the TP during JJAS. The features include the spatial similarity and the spatial standard deviation.

The output of the 1% to quadruple CO₂ experiment suggests that, in response to increased CO₂, the JJAS HS over the TP significantly increases (in the MME results of 1%CO₂, the area-averaged increase is 16.2 W m⁻²). Among the 4 months, the increase is the largest (~124 W m⁻²) in the southern TP in July; in other months, the magnitudes are slightly weaker. The HS increase does not seem to depend on the HS climatology over the TP. In terms of spatial pattern and TP-averaged results, the LH is mainly responsible for the increase in JJAS HS over the TP in response to increased CO₂. As the CO₂ concentration increases, the atmospheric humidity increases, with higher magnitude at lower levels. It enhances the vertical transportation of humidity. The moist air travels to higher level, in which the environmental temperature and saturated vapor pressure is lower. It results in the condensation of vapor and contributes to the increase in LH released to the atmospheric column. The TP surface warming induced by increased CO₂ leads to an enhancement of LH release to atmosphere at the surface, which also favors the HS increase. In addition, the atmospheric moisturizing may lead to absorption of upwelling longwave radiation from the surface and contribute to the HS increase.

Regarding the uncertainty of the models, the leading intermodel spread of the HS response to increased CO₂ is a mode with nearly uniform deviation across the TP; the second mode is a dipole structure, with the central TP and the southeastern TP in a seesaw structure. These two modes account for 53.6% of the total intermodel variance. Similar to the spatial pattern results, the LH is the main contributor to these two modes.

When CO₂ increase, the net radiation (intensified radiative cooling) slightly dampens the increases in the TP-averaged HS. The net radiation change is mainly contributed by the increases in both the downwelling longwave radiation flux at the surface and the upwelling longwave radiation flux at the top of the atmosphere. These changes are result from the CO₂-induced atmospheric warming over the TP.

The contribution of cloud–radiation feedback to the HS change over the TP is quite limited. It contributes little to the spatial pattern and the model uncertainty over the TP. Under a high-CO₂ scenario, it slightly offsets the enhancement of the downwelling longwave radiation at the TP surface but fails to significantly affect the HS response.

In addition, the climate system models have some limitation, which bring uncertainties to the CO₂-induced HS change over the TP. One is the snow cover. Among the CMIP5 models we chose, the snow cover data in these models are available: bcc-csm1-1, bcc-csm1-1-m, CanESM2, CESM1-BGC, CNRM-CM5, CNRM-CM5-2, CSIRO-Mk3-6-0, GISS-E2-H, GISS-E2-R, Inmcm4, MIROC-ESM, MIROC5, MPI-ESM-LR, MPI-ESM-MR, MPI-ESM-P, MRI-CGCM3, NorESM1-M and NorESM1-ME. Based on the data, it is found that the CMIP5 models tends to underestimate the snow cover over the TP during JJAS. For the climatological JJAS snow cover during 1971–1994 (the observational snow cover is only available during the period), the MME of CMIP5 historical simulation is 10.1%; the corresponding result in observation is 15.2%. It may slightly affect the energy balance over the TP. The vegetation change is also a limitation, which is not taken into consideration in 1%CO₂ experiment. The vegetation change may alter the albedo (as well as the shortwave and temperature) over the TP, adding uncertainty to the response results. Meanwhile, other factors may also affect the HS and its response, such as LH, sensible heating and other radiation fluxes (present study suggests the LH is the most important factor to the HS response). Considering that the MME of the CMIP5 models display a reasonable estimate of HS, the associated responses projected by the models are trustable.

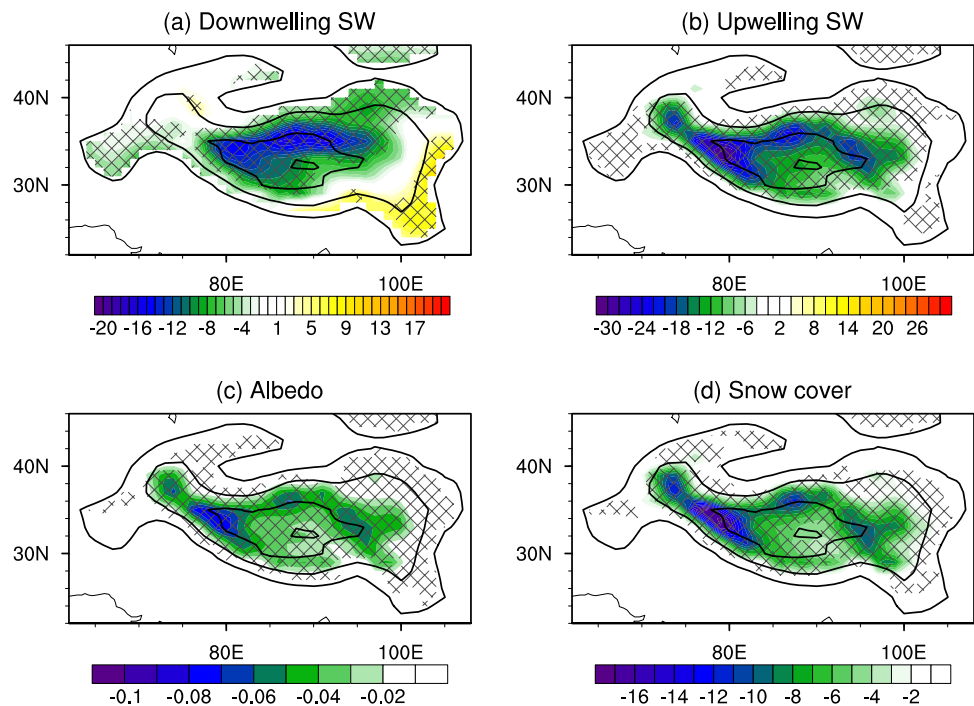
Acknowledgements We acknowledge the World Climate Research Programme's Working Group on Coupled Modelling, the climate modeling groups listed in Table 1 and the U.S. Department of Energy's Program for Climate Model Diagnosis and Intercomparison for making the CMIP5 output available for present analysis. Besides, the authors wish to thank four anonymous reviewers for the insightful comments that lead to a significant improvement to the manuscript. The study was supported by the Second Tibetan Plateau Scientific Expedition and Research (STEP) program (Grant no. 2019QZKK0102), the Strategic Priority Research Program of the Chinese Academy of Sciences (XDA20060501), the National Natural Science Foundation of China (41831175, 41530425) and Key Deployment Project of Centre for Ocean Mega-Research of Science, Chinese Academy of Sciences (COMS2019Q03).

Appendix: The responses of shortwave radiation fluxes

In response to increased CO₂, the increase of net shortwave radiation flux into the atmosphere column above the TP is 4.5 W m⁻². The detailed responses of the shortwave radiation fluxes are provided below:

The surface downwelling shortwave radiation flux In response to increased CO₂, this radiation flux decreases during JJAS. The TP-averaged decrease of the CMIP5 MME is 6.8 W m⁻² in the 1%CO₂ results (Fig. 3). The response of the downwelling shortwave radiation at the TP surface features

Fig. 11 The MME response (color shading) of JJAS downwelling shortwave radiation (**a** units: W m^{-2}), upwelling shortwave radiation (**b** units: W m^{-2}), albedo (**c** units: dimensionless) and snow cover (**d** units: %) at the surface for the 1%CO₂ results. The contours represent elevations of 1500, 3000, 5000 and 6000 m; the lattices indicate the response reaching the 95% significance level. Due to lack of data of snow cover, the following models are not participating in the calculation: ACCESS1-0, ACCESS1-3, BNU-ESM, CCSM4, FGOALS-s2, GFDL-CM3, GFDL-ESM2G, GFDL-ESM2M, HadGEM2-ES, IPSL-CM5A-LR, IPSL-CM5A-MR and IPSL-CM5B-LR



a dipole pattern, with a distinct decrease over the central TP and slight increase over the southeastern and northwestern TP (Fig. 11a). Comparison of the decrease in the all-sky results with the clear-sky results indicates that the inclusion of cloud–radiation feedback does not significantly alter the TP-averaged responses (Fig. 3), but enlarges the uncertainty. The fact that the clear-sky downwelling shortwave radiation uniformly decreases at the TP surface (figure not shown) implies that the inclusion of cloud–radiation feedback slightly modifies the response pattern of the downwelling shortwave radiation at the TP surface. For the reduction in the average of the downwelling shortwave radiation at the TP surface, the intensification of atmospheric absorption of shortwave may be responsible. This intensified absorption is probably led by atmosphere wetting. In response to increased CO₂, the moisture increases due to the atmospheric warming. The water vapor is able to absorb shortwave (Yang et al. 2006).

The surface upwelling shortwave radiation flux Meanwhile, this shortwave radiation flux decreases more than the downwelling shortwave radiation. In the 1%CO₂ results, the averaged surface upwelling shortwave radiation of the CMIP5 MME over the TP decreases by 12.1 W m^{-2} (Fig. 3). The response of the upwelling shortwave radiation features a nearly uniform weakening at the TP surface (Fig. 11b). The weakening is relatively large at elevations above 3000 m. The upwelling shortwave radiation at the surface is mainly the reflection of the downwelling shortwave radiation. The larger change in the upwelling shortwave radiation than that of the downwelling shortwave radiation indicates that the

albedo of the TP surface changes. The albedo of the TP also uniformly reduces, with relatively large magnitude above 3000 m (Fig. 11c). The response pattern of snow cover is almost the same as that of albedo, with the spatial correlation coefficient between them being 0.94. This means that the shrinking of snow cover in response to increased CO₂ leads to a reduction in albedo as well as the upwelling shortwave radiation at the TP surface. The inclusion of cloud–radiation feedback may slightly enhance the overall upwelling shortwave radiation at the TP surface, but the enhancement is statistically insignificant (Fig. 3).

The outgoing shortwave radiation flux at the top of the atmosphere Over the TP, this outgoing radiation flux reduces significantly. In the 1%CO₂ results, the TP-averaged magnitude of the CMIP5 MME is 9.6 W m^{-2} (Fig. 3). The TP displays a uniform decrease in this radiation, with relatively large magnitude over the western TP at elevations between 3000 and 5000 m (Fig. 12). The response pattern is similar to that of the upwelling shortwave radiation at the TP surface (Fig. 11b), with a spatial correlation coefficient of 0.63 between the two. It indicates that the reduction of the outgoing shortwave radiation is mainly led by the change in the upwelling shortwave radiation at the TP surface. The discrepancies in the detail may be caused by the masking effect of cloud or the atmospheric absorption to shortwave. Overall, the model results suggest that the inclusion of cloud–radiation feedback may not significantly affect the response of the TP-averaged outgoing shortwave radiation (Fig. 3). But it is important to note that the change in radiative fluxes at the top of atmosphere, resulting from the

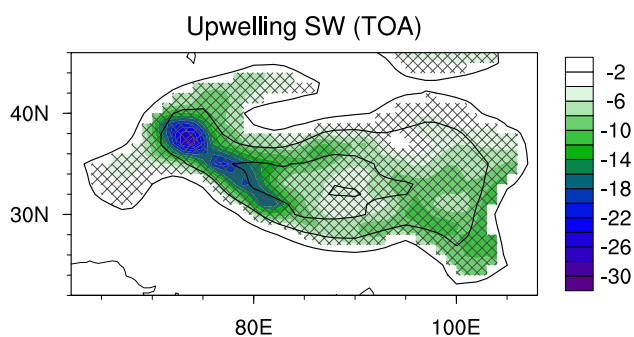


Fig. 12 The MME response (color shading) of JJAS upwelling short-wave radiation (units: W m^{-2}) at the top of the atmosphere for the 1% CO_2 results. The contours represent elevations of 1500, 3000, 5000 and 6000 m; the lattices indicate the response reaching the 95% significance level

cloud-radiation feedback, is the largest source of uncertainty in the climate response to CO_2 forcing simulated by GCMs because of the unrealistic presentation of cloud processes in the models.

The downwelling shortwave radiation flux at the top of the atmosphere It is not analyzed because it barely changes (Fig. 3).

References

- Abe M, Hori M, Yasunari T, Kitoh A (2013) Effects of the Tibetan Plateau on the onset of the summer monsoon in South Asia: the role of the air-sea interaction. *J Geophys Res Atmos* 118(4):1760–1776. <https://doi.org/10.1002/jgrd.50210>
- Adler RF, Huffman GJ, Chang A, Ferraro R, Xie P-P, Janowiak J, Rudolf B, Schneider U, Curtis S, Bolvin D (2003) The version-2 global precipitation climatology project (GPCP) monthly precipitation analysis (1979–present). *J Hydrometeorol* 4(6):1147–1167
- Becker A, Finger P, Meyer-Christoffer A, Rudolf B, Schamm K, Schneider U, Ziese M (2013) A description of the global land-surface precipitation data products of the Global Precipitation Climatology Centre with sample applications including centennial (trend) analysis from 1901–present. *Earth Syst Sci Data* 5(1):71–99. <https://doi.org/10.5194/essd-5-71-2013>
- Boos WR, Kuang Z (2010) Dominant control of the South Asian monsoon by orographic insulation versus plateau heating. *Nature* 463(7278):218–222
- Byrne MP, O’Gorman PA (2016) Understanding decreases in land relative humidity with global warming: conceptual model and GCM simulations. *J Clim* 29(24):9045–9061. <https://doi.org/10.1175/jcli-d-16-0351.1>
- Chou C, Neelin JD, Chen CA, Tu JY (2009) Evaluating the “rich-get-richer” mechanism in tropical precipitation change under global warming. *J Clim* 22(8):1982–2005
- Du Y, Xie SP, Huang G, Hu K (2009) Role of air–sea interaction in the longpersistence of El Niño-induced North Indian Ocean warming. *J Clim* 22(8):2023–2038
- Duan AM, Wu GX (2008) Weakening trend in the atmospheric heat source over the Tibetan Plateau during recent decades. Part I: observations. *J Clim* 21:3149–3164
- Duan AM, Wu GX (2009) Weakening trend in the atmospheric heat source over the Tibetan Plateau during recent decades Part II: connection with climate warming. *J Clim* 22(15):4197–4212. <https://doi.org/10.1175/2009jcli2699.1>
- Endo H, Kitoh A (2014) Thermodynamic and dynamic effects on regional monsoon rainfall changes in a warmer climate. *Geophys Res Lett* 41(5):1704–1710. <https://doi.org/10.1002/2013gl059158>
- He B, Liu YM, Wu GX, Wang ZQ, Bao Q (2019a) The role of air-sea interactions in regulating the thermal effect of the Tibetan-Iranian Plateau on the Asian summer monsoon. *Clim Dyn* 52(7–8):4227–4245. <https://doi.org/10.1007/s00382-018-4377-y>
- He C, Wang Z, Zhou T, Li T (2019b) Enhanced latent heating over the Tibetan Plateau as a key to the enhanced East Asian summer monsoon circulation under a warming climate. *J Clim* 32(11):3373–3388. <https://doi.org/10.1175/jcli-d-18-0427.1>
- Held IM, Soden BJ (2006) Robust responses of the hydrological cycle to global warming. *J Clim* 19(21):5686–5699. <https://doi.org/10.1175/Jcli3990.1>
- Hu Q, Jiang D, Fan G (2015) Climate change projection on the Tibetan Plateau: results of CMIP5 models. *Chin J Atmos Sci* 2:42–52. <https://doi.org/10.3878/j.issn.1006-9895.1406.13325>
- Huang J, Wang T, Wang W, Li Z, Yan H (2014) Climate effects of dust aerosols over East Asian arid and semiarid regions. *J Geophys Res Atmos* 119(19):11398–11416. <https://doi.org/10.1002/2014jd021796>
- Huang J, Ma J, Guan X, Li Y, He Y (2019) Progress in semi-arid climate change studies in China. *Adv Atmos Sci* 36(9):922–937. <https://doi.org/10.1007/s00376-018-8200-9>
- Kamae Y, Ogura T, Watanabe M, Xie SP, Ueda H (2016) Robust cloud feedback over tropical land in a warming climate. *J Geophys Res Atmos* 121(6):2593–2609. <https://doi.org/10.1002/2015jd024525>
- Kanamitsu M, Ebisuzaki W, Woollen J, Yang SK, Hnilo JJ, Fiorino M, Potter GL (2002) NCEP-DOE AMIP-II reanalysis (R-2). *Bull Am Meteor Soc* 83(11):1631–1643. <https://doi.org/10.1175/bams-83-11-1631>
- Kang L, Huang J, Chen S, Wang X (2016) Long-term trends of dust events over Tibetan Plateau during 1961–2010. *Atmos Environ* 125:188–198. <https://doi.org/10.1016/j.atmosenv.2015.10.085>
- Kitoh A (2004) Effects of mountain uplift on East Asian Summer Climate investigated by a coupled atmosphere ocean GCM. *J Clim* 17(4):783–802
- Kobayashi S, Ota Y, Harada Y, Ebata A, Morioka M, Onoda H, Onogi K, Kamahori H, Kobayashi C, Endo H, Miyaoka K, Takahashi K (2015) The JRA-55 Reanalysis: general specifications and basic characteristics. *J Meteor Soc Japan* 93(1):5–48. <https://doi.org/10.2151/jmsj.2015-001>
- Laine A, Nakamura H, Nishii K, Miyasaka T (2014) A diagnostic study of future evaporation changes projected in CMIP5 climate models. *Clim Dyn* 42(9–10):2745–2761. <https://doi.org/10.1007/s00382-014-2087-7>
- Lee JY, Wang B, Seo KH, Ha KJ, Kitoh A, Liu J (2015) Effects of mountain uplift on global monsoon precipitation. *Asia-Pacific J Atmos Sci* 51(3):275–290. <https://doi.org/10.1007/s13143-015-0077-2>
- Li C, Yanai M (1996) The onset and interannual variability of the Asian summer monsoon in relation to land-sea thermal contrast. *J Clim* 9(2):358–375. <https://doi.org/10.1175/1520-0442>
- Li XQ, Ting MF, Li CH, Henderson N (2015) Mechanisms of Asian summer monsoon changes in response to anthropogenic forcing in CMIP5 models. *J Clim* 28(10):4107–4125. <https://doi.org/10.1175/jcli-d-14-00559.1>
- Liu Y, Hoskins B, Blackburn M (2007) Impact of Tibetan orography and heating on the summer flow over Asia. *J Meteor Soc Japan* 85:1–19. <https://doi.org/10.2151/jmsj.85B.1>
- Luo H, Yanai M (1984) The large-scale circulation and heat sources over the Tibetan plateau and surrounding areas during the early

- summer of 1979. Part II: heat and moisture budgets. *Mon Weather Rev* 112(5):966–989
- O’Gorman PA, Muller CJ (2010) How closely do changes in surface and column water vapor follow Clausius–Clapeyron scaling in climate change simulations? *Environ Res Lett*. <https://doi.org/10.1088/1748-9326/5/2/025207>
- Qu X, Huang G, Zhu L (2019) The CO₂-induced sensible heat changes over the Tibetan Plateau from November to April. *Clim Dyn* 53(9–10):5623–5635. <https://doi.org/10.1007/s00382-019-04887-x>
- Riahi K, Rao S, Krey V, Cho C, Chirkov V, Fischer G, Kindermann G, Nakicenovic N, Rafaj P (2011) RCP 8.5—a scenario of comparatively high greenhouse gas emissions. *Clim Change* 109(1–2):33–57. <https://doi.org/10.1007/s10584-011-0149-y>
- Robinson DA, Dewey KF, Heim RR (1993) Global snow cover monitoring: an update. *Bull Am Meteor Soc* 74(9):1689–1696. [https://doi.org/10.1175/1520-0477\(1993\)074%3c1689:Gscmau%3e2.0.Co;2](https://doi.org/10.1175/1520-0477(1993)074%3c1689:Gscmau%3e2.0.Co;2)
- Sampe T, Xie SP (2010) Large-scale dynamics of the Meiyu-Baiu Rainband: environmental forcing by the westerly jet. *J Clim* 23(1):113–134. <https://doi.org/10.1175/2009JCLI3128.1>
- Song JH, Kang HS, Byun YH, Hong SY (2010) Effects of the Tibetan Plateau on the Asian summer monsoon: a numerical case study using a regional climate model. *Int J Climatol* 30(5):743–759. <https://doi.org/10.1002/joc.1906>
- Stocker TF, Qin D, Plattner GK, Alexander LV, Allen SK, Bindoff NL, Bréon FM, Church JA, Cubasch U, Emori S (2013) Technical summary. In: Stocker TF, Qin D, Plattner G-K et al (eds) *Climate Change 2013: The Physical Science Basis. Contribution of Working Group I to the Fifth Assessment Report of the Intergovernmental Panel on Climate Change*. Cambridge University Press, Cambridge, United Kingdom and New York, NY, USA, p 79
- Su F, Duan X, Chen D, Hao Z, Cuo L (2013) Evaluation of the global climate models in the CMIP5 over the Tibetan Plateau. *J Clim* 26(10):3187–3208. <https://doi.org/10.1175/jcli-d-12-00321.1>
- Taylor KE (2001) Summarizing multiple aspects of model performance in a single diagram. *J Geophys Res Atmos* 106(D7):7183–7192
- Taylor KE, Stouffer RJ, Meehl GA (2012) An overview of CMIP5 and the experiment design. *Bull Am Meteor Soc* 93(4):485–498. <https://doi.org/10.1175/BAMS-D-11-00094.1>
- Thomson AM, Calvin KV, Smith SJ, Kyle GP, Volke A, Patel P, Delgado-Arias S, Bond-Lamberty B, Wise MA, Clarke LE (2011) RCP4 5: a pathway for stabilization of radiative forcing by 2100. *Clim Change* 109(1):77–94
- Wang B, Ding Q (2008) Global monsoon: dominant mode of annual variation in the tropics. *Dyn Atmos Oceans* 44(3–4):165–183. <https://doi.org/10.1016/j.dynatmoce.2007.05.002>
- Wang B, Wu R, Lau KM (2001) Interannual variability of the Asian summer monsoon: contrasts between the Indian and the western North Pacific-east Asian monsoons. *J Clim* 14(20):4073–4090. [https://doi.org/10.1175/1520-0442\(2001\)014%3c4073:Ivotas%3e2.0.Co;2](https://doi.org/10.1175/1520-0442(2001)014%3c4073:Ivotas%3e2.0.Co;2)
- Wang H, Xie SP, Kosaka Y, Liu QY, Du Y (2019) Dynamics of Asian summer monsoon response to anthropogenic aerosol forcing. *J Clim* 32(3):843–858. <https://doi.org/10.1175/jcli-d-18-0386.1>
- Wu G, Liu Y, He B, Bao Q, Duan A, Jin FF (2012) Thermal controls on the Asian summer monsoon. *Sci Rep* 2:404. <https://doi.org/10.1038/srep00404>
- Yang K, Koike T, Ye BS (2006) Improving estimation of hourly, daily, and monthly solar radiation by importing global data sets. *Agric For Meteorol* 137(1–2):43–55. <https://doi.org/10.1016/j.agrfor.2006.02.001>
- Yao TD, Thompson L, Yang W, Yu WS, Gao Y, Guo XJ, Yang XX, Duan KQ, Zhao HB, Xu BQ, Pu JC, Lu AX, Xiang Y, Kattel DB, Joswiak D (2012) Different glacier status with atmospheric circulations in Tibetan Plateau and surroundings. *Nat Clim Change* 2(9):663–667. <https://doi.org/10.1038/Nclimate1580>
- Ye D-Z, Wu G-X (1998) The role of the heat source of the Tibetan Plateau in the general circulation. *Meteorol Atmos Phys* 67(1–4):181–198
- Zhao Y, Duan AM, Wu GX, Sun RZ (2019) Response of the Indian Ocean to the Tibetan Plateau thermal forcing in late spring. *J Clim* 32(20):6917–6938. <https://doi.org/10.1175/jcli-d-18-0880.1>

Publisher’s Note Springer Nature remains neutral with regard to jurisdictional claims in published maps and institutional affiliations.